Performance of high-resolution PET detectors based on long semi-monolithic scintillator slabs*

Samuel Mungai Kinyanjui,[1,2] Zhonghua Kuang,[1,3] Zheng Liu,[1] Ning Ren,[1] and Yongfeng Yang[1,†]

[1]*Paul C. Lauterbur Research Center for Biomedical Imaging Shenzhen Institutes of Advanced Technology, Chinese Academy of Sciences, Shenzhen 518055, China*

[2]*Shenzhen College of Advanced Technology, University of Chinese Academy of Sciences, Shenzhen 518055, China*

[3]*Microelectronics and Optoelectronics Technology Key Laboratory of Hunan Higher Education, School of Physics and Electronic Electrical Engineering, Xiangnan University, Chenzhou 423000, China*

Conventional positron emission tomography (PET) scanners use either highly-segmented or monolithic scintillator detectors. Depth of interaction (DOI) information is vital for high-resolution PET scanners using either segmented scintillator detectors with a large aspect ratio of crystal length to width or monolithic scintillator detectors with a large ratio of crystal thickness to spatial resolution. Semi-monolithic scintillator detectors maintain the intrinsic DOI encoding capability of monolithic detectors and meanwhile, the edge effect is much smaller. The objective of this study is to compare the performance of semi-monolithic scintillator detectors with different slab thicknesses, slab surface treatments, and reflector types. Four long semi-monolithic detectors consisting of lutetium yttrium oxyorthosilicate (LYSO) slabs of $0.96 \times 56 \times 10\,\mathrm{mm}^3$ and $0.81 \times 56 \times 10\,\mathrm{mm}^3$, with and without black paint at both end and front surfaces were measured. Additionally, semi-monolithic detectors using either barium sulfate ($BaSO_4$) or enhanced specular reflector (ESR) as the inter-slab reflector were compared for the first time. The semi-monolithic detectors were read out by 4×16 silicon photomultiplier (SiPM) array with a row and column summing readout circuit and the signals were processed using electronics developed in our lab. Black paint treatment of the two end and front surfaces degrades the energy resolution but improves both the spatial resolution in the monolithic direction and DOI resolution, thus improving the overall performance of the detector. The detector using ESR reflector provides clearer individual slab identification in the flood histogram, similar spatial resolution in the monolithic direction, DOI resolution, and energy resolution. The squared centroid of gravity (squared COG) method improves the spatial resolution in the monolithic direction by ~30% as compared to the COG method. The long semi-monolithic scintillator detectors optimized in this work provide a clear identification of LYSO slabs of 0.96 and $0.81\,\mathrm{mm}$ thick, a spatial resolution in the monolithic direction of ~$1.7 \pm 0.3\,\mathrm{mm}$, a DOI resolution of ~$2.1 \pm 0.7\,\mathrm{mm}$, and an energy resolution of ~$17.5 \pm 2.0\%$. The detectors can be used to develop high-performance small animal and organ-specific PET scanners in the future.

Keywords: Positron emission tomography (PET), PET detector, semi-monolithic scintillator, silicon photomultiplier (SiPM), depth of interaction (DOI).

I. INTRODUCTION

Positron emission tomography (PET) is a non-invasive medical imaging tool used for early detection of many major diseases like cancer[1, 2]. Achieving high spatial resolution in a PET scanner allows for the accurate measurement of biochemical processes in the organs and tissues of living subjects by reducing the partial volume effect[3]. This is particularly important for small animal imaging [4–6] and some clinical applications such as neuroimaging [7].

Depth of interaction (DOI) uncertainty deteriorates the spatial resolution of PET scanners, particularly for small animal and organ-specific PET scanners that use detectors with a high aspect ratio of crystal length to width [6, 8]. Due to crystal penetration, events may be incorrectly assigned to the wrong line of response when using detectors that lack DOI measurement or have poor DOI resolution. The error resulting from DOI uncertainty rises as the crystal's aspect ratio increases. In the most common cylindrical detector geometry, this DOI uncertainty error grows with both the radial offset and the ring difference. DOI encoding in PET detectors is important for a PET scanner to achieve a uniformly high spatial resolution.

Currently, the state of the art PET scanners use either pixelated or monolithic scintillator crystals read out by silicon photomultiplier (SiPM) photodetectors. Pixelated detectors can achieve a high timing resolution since the scintillation photons are constrained in a smaller area and the photodetector can achieve a high signal-to-noise ratio. They can also achieve superior planar position resolution by using small scintillator crystals [9, 10]. DOI information however is not intrinsically present in pixelated detectors and modified detector designs such as dual-ended readout or multiple-layer crystals are required to measure the DOI, which increase the costs and complexity of the detectors [11–15]. The pixelated detectors also have lower detection efficiency due to the dead-space occupied by the inter-crystal reflectors [5]. In the

* This work was supported in part by the National Natural Science Foundation of China (No. 62101539, 12375358), the Basic Research Program of Shenzhen (No. JCYJ20220818101612027), the Natural Science Foundation of Hunan Province (No. 2024JJ6414), the Key Laboratory of Biomedical Imaging Science and System, Chinese Academy of Sciences, and the Key Laboratory for Magnetic Resonance and Multimodality Imaging of Guangdong Province (No. 2023B1212060052).

Samuel Mungai Kinyanjui and Zhonghua Kuang have contributed equally to this work.

† Corresponding author , yf.yang@siat.ac.cn

monolithic scintillator detectors, the DOI information is intrinsically presented as it can be extracted from the scintillation photon distribution [5, 7]. The efficiency of the monolithic detectors is superior and the cost is lower as compared to the pixelated detectors. The monolithic detectors have the disadvantage of large edge effect. Due to the loss and reflection of the scintillation photons at the edge of the detector, fewer scintillation photons are detected and the measured planar positions are compressed for the interactions happening close to the edge of the detector, resulting in a degradation of both the planar and DOI resolutions. Both the planar spatial resolution and DOI resolutions deteriorate and the edge effect increases as the detector thickness increases [16–23].

The semi-monolithic scintillator detectors harness the advantages of both pixilated and monolithic scintillator detectors. They still maintain the inherent DOI encoding capability although the scintillation photon distribution is limited to fewer photosensors along the monolithic direction. As compared to the monolithic detectors, the semi-monolithic detectors have a smaller edge effect and which can be further reduced by using longer scintillator slabs. The semi-monolithic scintillator PET detectors were proposed and preliminary evaluated using detectors consisting of one or a few scintillator slabs by Chung et al [24, 25] around 2010. Later, the least-square minimization and the maximum likelihood positioning algorithms were developed [26] and the slab surface treatments were optimized [27, 28] by our group for semi-monolithic detectors. More recently, more works were performed on developing semi-monolithic detectors for small animal [29], dedicated brain, and whole body [30–32] PET scanners. It was also found that machine learning-based positioning algorithms can improve both the spatial resolution in monolithic direction and DOI resolutions, as well as reduce the edge effect [32–34].

In this work, four semi-monolithic detectors using long LYSO slab arrays of different slab surface treatments, slab thicknesses, and inter-slab reflectors will be evaluated. The performance of semi-monolithic detector using two different inter-slab reflectors will be compared for the first time. The positioning resolution of the monolithic direction obtained using the conventional centroid of gravity (COG) and squared COG algorithms will also be compared.

II. MATERIALS AND METHODS

A. Detector modules

Fig. 1 shows a schematic of a detector module. The detector module was composed of LYSO slabs read out by a SiPM array with a lightguide in between them. Table 1 shows detailed parameters of the 4 detector modules measured in this work. The semi-monolithic LYSO arrays were manufactured by the Epic Crystal Co. (Shanghai, China). The reflector in between individual slabs of detectors 1, 2, and 4 was barium sulfate ($BaSO_4$), while the enhanced specular reflector (ESR) of 3M Company was used in detector 3. The thickness of the $BaSO_4$ and the thickness of the ESR plus optical glue were both $0.08\,\mathrm{mm}$. The optical glue is the EPO-TEK 301 from EXPOXY Technology INC. (MA, USA). For detectors 1, 3, and 4, the two end and front surfaces were unpolished and painted with a black marker pen, and the surfaces of detector 2 were unpolished and left unpainted. For all the detectors, the two large surfaces of each slab and the bottom surface interfacing with the readout SiPM were polished. Each detector module was read out by a 4×16 SiPM array coupled to the bottom of the LYSO array. The SiPM array was composed of 64 single SiPM pixels (S14160-3050HS of Hamamatsu Inc., Hamamatsu, Japan). Each single SiPM has a size of $3.4 \times 3.4\,\mathrm{mm}^2$ and an active area of $3 \times 3\,\mathrm{mm}^2$. The pitch of the SiPM array is $3.65\,\mathrm{mm}$. All measurements were performed at a SiPM bias voltage of $44.5\,\mathrm{V}$. The lightguide was made of $1.5\,\mathrm{mm}$ thick k9 glass with a refractive index of 1.51.

To enhance the slab identification, two edge grooves of $0.2\,\mathrm{mm}$ wide and $1\,\mathrm{mm}$ deep were cut on the lightguide. The grooves were filled with the $BaSO_4$ reflector. For detectors 1 to 3, the grooves were $1.91\,\mathrm{mm}$ away from both edges. For detector 4, the grooves were $2.05\,\mathrm{mm}$ from both edges. Optical grease with a refractive index of 1.41 was used in between both the lightguide and the scintillator slab array and the lightguide and the SiPM array.

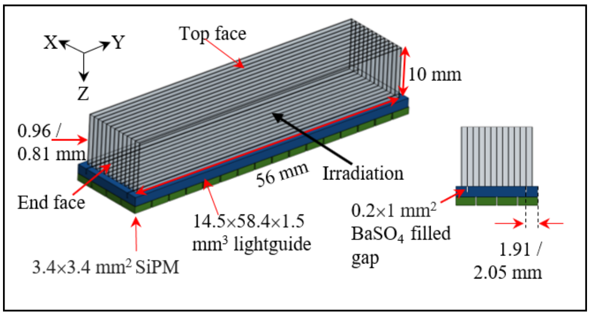

Fig. 1. Schematic of a detector module showing the dimensions for all components. The detector module is composed of 12 or 14 thin LYSO scintillator slabs separated by reflector and read out by a SiPM array.

Table 1. Parameters of the 4 distinct detectors used in this work.

Detector No.	No. of slabs	Size of the slabs (mm^3)	Front & end surfaces treatement	Inter-slab reflector
1	12	$0.96 \times 56 \times 10$	painted	$BaSO_4$
2	12	$0.96 \times 56 \times 10$	unpainted	$BaSO_4$
3	12	$0.96 \times 56 \times 10$	painted	ESR
4	14	$0.81 \times 56 \times 10$	painted	$BaSO_4$

B. Experimental setup

The experimental setup is shown in Fig. 2. All measurements were conducted in a light-tight chamber made of plastic and covered with a black cloth, and the operating temperature for the detectors was $14\,^{\circ}\mathrm{C}$. The flood histogram was

measured by placing a $0.3\,\mathrm{mm}$ diameter ^{22}Na point source with an activity of $165\,\mathrm{kBq}$ $24\,\mathrm{mm}$ away from one lateral face of the detector. The monolithic direction spatial, DOI, and energy resolution measurements were all done in coincidence with a reference detector. The reference detector was a single LYSO crystal of $1 \times 1 \times 20\,\mathrm{mm}^3$ wrapped with Teflon and read out by a single Hamamatsu S14160-3050HS SiPM with an active area of $3 \times 3\,\mathrm{mm}^2$. A collimated $511\,\mathrm{keV}$ beam was produced by placing the ^{22}Na point source in between the reference detector and a $5\,\mathrm{mm}$ thick tungsten collimator with a $1\,\mathrm{mm}$ diameter hole drilled. The $1\,\mathrm{mm}$ hole of the collimator, the ^{22}Na point source, and the reference detector were well aligned and placed on a motorized translational platform. The semi-monolithic detector under test was placed on a stationary platform. The translational platform can move in both the monolithic direction (y axis) and DOI direction (z axis spanning from the top of the detector to the SiPM array). The semi-monolithic scintillator detector was irradiated from a series (y, z) positions by moving the translational platform. As shown in the top of Fig. 3, detectors 1 and 4 were irradiated for 27×5 positions starting $2\,\mathrm{mm}$ from one end and $1\,\mathrm{mm}$ from the front with a stepping size of $2\,\mathrm{mm}$ in both the monolithic and DOI directions. To save the measurement time, detectors 2 and 3 were only irradiated for 27 y positions along the center z and 5 z positions along the middle y as shown in the bottom of Fig. 3 and only results from those positions were used to compare the performance of the four detectors. The irradiation time for each position was $2200\,\mathrm{s}$. The percentage of the useful coincidence events to the total singles events is ~0.02% for an energy window of 350-650 keV for both detectors.

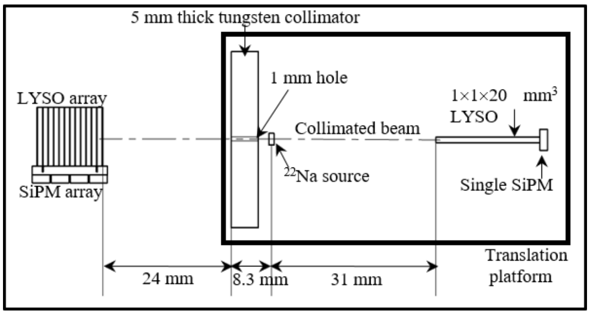

Fig. 2. The experimental setup for the coincidence measurements.

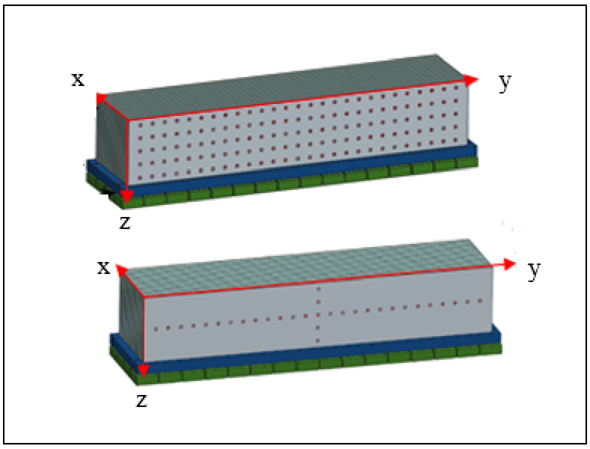

Fig. 3. The irradiation positions for (top) detectors 1 and 4, and (bottom) detectors 2 and 3.

C. Electronics and data acquisition

The 64 signals from the SiPM array were aggregated by a row-column summing circuit to form 4 row and 16 column signals as shown in Fig. 4. The 4 row signals were used for slab identification (x). The 16 column signals were used for both the y and z position measurements.

The 20 signals were propagated to a preamplifier board, where all signals were first amplified by voltage feedback amplifiers (model AD8056, Analog Devices, MA, USA). A timing signal was produced by summing the 4 pre-amplified row signals. The timing signal was further amplified by a fast amplifier (model AD8045, Analog Devices, MA, USA). A $50\,\mathrm{mV}$ threshold signal was used together with the timing signal to generate 3 differential timing signal pairs by 3 high-speed comparators (model ADCMP604, Analog Devices, MA, USA) independently.

The 3 differential timing signal pairs and the 20 energy signals of the test detector, as well as 1 differential timing signal pair and 1 energy signal of the reference detector were propagated by micro-coaxial cables to a singles processing unit (SPU) originally developed for our SIAT bPET scanner [35]. as shown in Fig. 5. The SPU board can process 8 independent dual-ended readout detectors with each containing 8 energies and one differential timing signal pair. Three and one SPU electronics blocks were used to read out the test and reference detectors, respectively.

In the SPU, first, the energy signals from the preamplifier boards were shaped and amplified. Second, the waveforms of the energy signals were sampled at a rate of $62.5\,\mathrm{MHz}$ by analog-to-digital converters (ADCs). Third, the digital signals were processed in a field-programmable gate array (FPGA) to determine the signal energies by calculating the areas under the waveforms. This was done by summing 18 waveform samples and subtracting the baseline, which is the average of 4 samples taken before the waveform's rising edge. For each electronic block, a differential timing pair is sent to a tapped delay line time-to-digital converter (TDC) to obtain the timestamp of an event, which is also used as the starting signal for the area calculation of the energy. Finally, from each SPU electronics block, eight energy values and a timestamp for each event are sent to the host PC using an Ethernet-based User Datagram Protocol (UDP) [36–39].

Software-based data selection and coincidence processing were completed on the host PC. A coincidence timing window of $10\,\mathrm{ns}$ was used. The coincidence data containing 20 energies of the test detector and the time difference between the reference detector and the test detector was stored as list-mode data and used for further analysis.

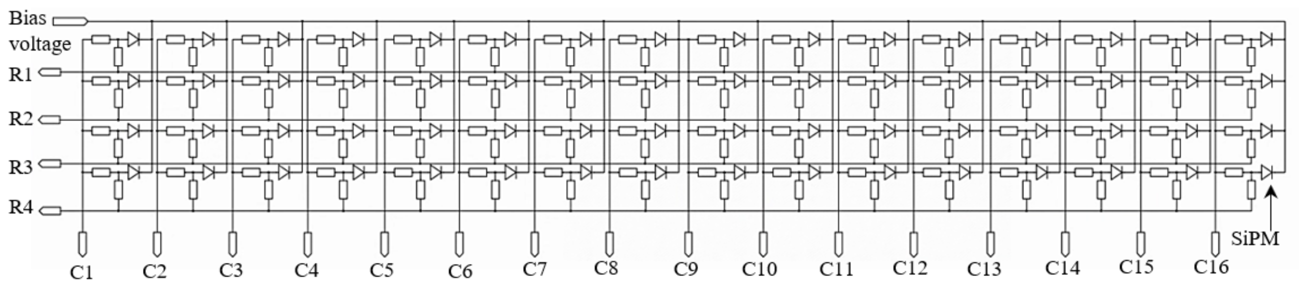

Fig. 4. The row-column resistor network readout circuit of the 4×16 SiPM array. R represents the rows while C represents the columns. All resistors are 200 Ω.

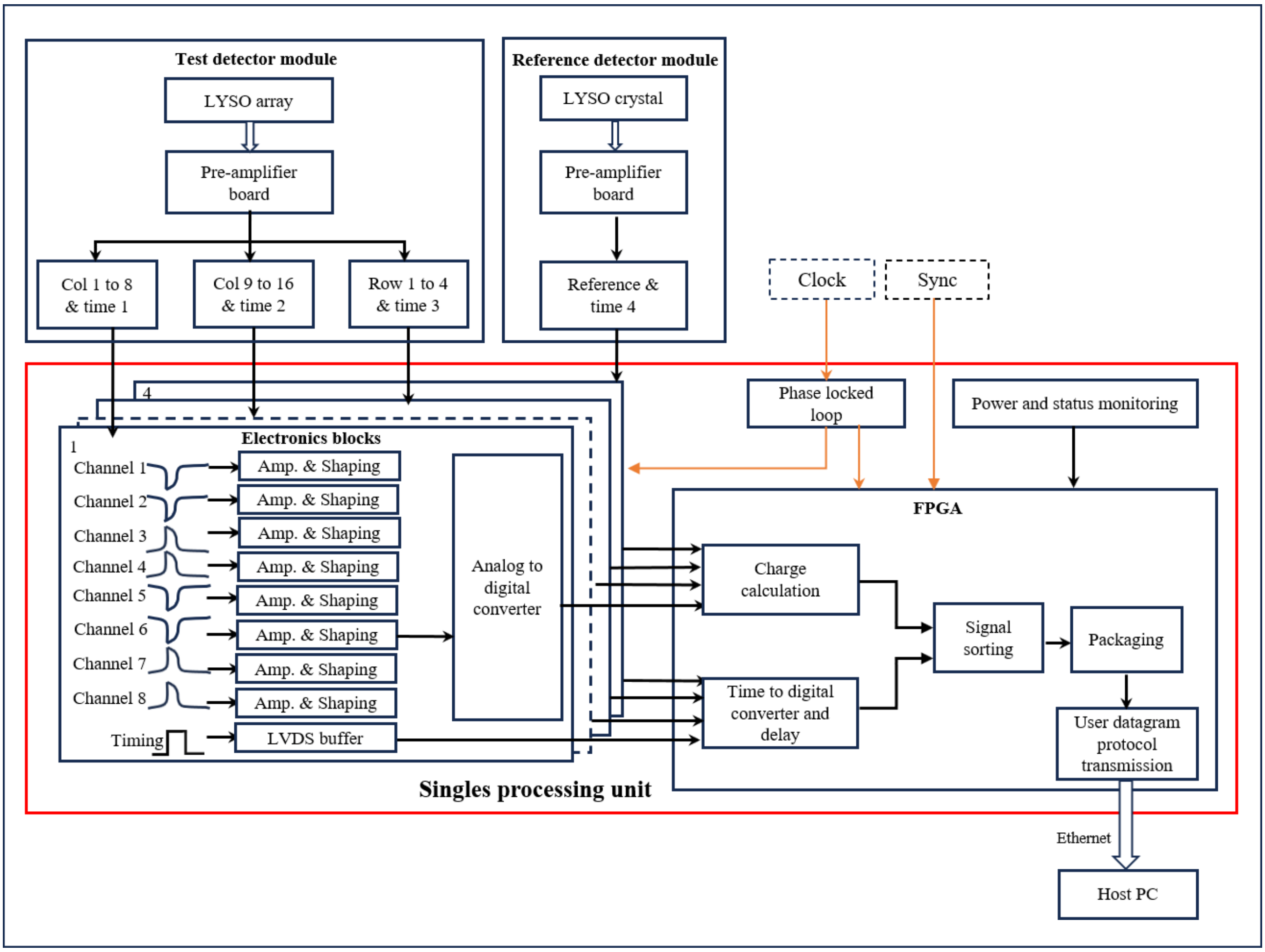

Fig. 5. Schematic of the signal processing electronics system.

D. Data analysis

1. Planar position

The (x) and (y) coordinates of the interaction are calculated by the conventional COG algorithm as the following:

$$x = \frac{\sum_{j=1}^{4} j \times q_j}{5\sum_{j=1}^{4} q_j} \tag{1}$$

$$y = \frac{\sum_{i=1}^{16} i \times q_i}{17 \sum_{i=1}^{16} q_i} \tag{2}$$

The (y) coordinate is also calculated with a squared COG algorithm as the following:

$$y = \frac{\sum_{i=1}^{16} i \times q_i^2}{17 \sum_{i=1}^{16} q_i^2} \tag{3}$$

Where i is the column number of the signals and q_i is the amplitude of the i-th column signal. The j is the row number of the signals and q_j is the amplitude of the j-th row signal. From the calculated x, y coordinates, a flood histogram showing the 2D distribution of the gamma interaction positions in a detector can be plotted to show the slab identification of the detector. The flood histogram can be segmented to obtain a slab look-up table, which can be used later to assign events to different slabs. For the coincidence measurement of irradiation of a specific (y, z) position of the detector, histograms of y coordinates can be obtained for individual slabs by using either the COG or squared COG algorithms [40]. The histograms are fitted with a Gaussian function to obtain the peak positions. For each (y, z) position, a peak position of the y histograms is determined as the average of all slabs. The curve of the peak positions and the true y irradiation position values of a specific z is fitted with a cubic polynomial function to obtain the fitting parameters. The measured y histogram of each (y, z) position can be converted from pixel value to mm by using the fitting parameters. The converted y histograms are then fitted with Gaussian functions and the FWHM y resolutions are obtained for all measured positions.

2. *Energy*

The energy of the detector is calculated by summing the amplitudes of the 16 column signals. The energy histograms of each irradiation position are populated for all individual slabs. A Gaussian fitting is performed and the energy resolution is calculated as a ratio of the FWHM to the mean.

3. *DOI*

The DOI of a gamma interaction is estimated using the inverse standard deviation of the amplitudes of the 16 column signals as shown in equation (4):

$$\mathrm{DOI} = \frac{1}{\sqrt{\frac{1}{16}\sum_{i=1}^{16}\left(q_{ni} - \bar{q}_n\right)^2}} \tag{4}$$

Where q_{ni} is the normalized amplitude of the i-th column signal and $\bar{q}_n$ is the average amplitude of the 16 column signals. 5 DOI histograms of each y position can be obtained for each slab and Gaussian fittings are performed to obtain the FWHMs and peak positions of the histograms. The FWHM is converted to mm by using the peak positions of the neighboring DOI histograms and the known DOI interval of $2\,\mathrm{mm}$. An energy window of 350-650 keV is used for all results of this work. The irradiation beam width that is estimated to be ~$1\,\mathrm{mm}$ is not subtracted from the y and DOI resolutions.

4. *Timing*

The timing of the detector is the timing difference between the reference detector and the test detector. The timing spectra of each irradiation position are populated for all individual slabs using a timing window of $40\,\mathrm{ns}$. A Gaussian fitting is performed and FWHM timing resolution can be obtained.

III. RESULTS

A. Flood histograms

The flood histograms of the 4 detectors are shown in Fig. 6. The flood histograms show the x and y positions of the gamma rays' interactions with the detectors, with the grayscale value of the color bar representing the number of interactions occurring at those positions. A profile through the middle of each flood histogram is also shown in Fig. 6. The average peak-to-valley ratios of the 4 detectors are 3.03 ± 0.96, 4.67 ± 1.29, 5.04 ± 1.44, and 2.58 ± 0.85, respectively. All slabs were clearly resolved for detectors 1-3 using $0.96\,\mathrm{mm}$ thick slabs. As seen in the flood histogram, along the x coordinate of the detector, the slab identification was best achieved in detector 3 which used the ESR reflector. The second and third slabs near the edges could not be clearly resolved for detector 4 using $0.81\,\mathrm{mm}$ thick slabs. Probably the positions of the cuts in the lightguide need to be further optimized. Black painting the two end and front surfaces of the slabs reduced the scintillation photon reflection at those surfaces and mainly resulted in longer flood histograms in the monolithic direction that implies a better y position resolution, while the slab identification was almost unchanged.

B. Energy resolution

The energy spectra of a middle slab of the 4 detectors measured at 5 DOIs are shown in Fig. 7. Detector 3 which uses the specular ESR reflector has the lowest light output, but the photopeak amplitudes do not change with the depths. The other 3 detectors that use the diffusive $BaSO_4$ reflector have much higher light output, but the photopeak amplitude significantly changes with the depths. Depth-dependent energy calibration will be required for those detectors. The average energy resolution of detectors 1 and 4 measured for the 27×5 (y, z) positions are shown in table 2. Average energy resolutions of 17.4% and 17.6% are achieved for the two detectors, respectively, which implies that the thickness of the slab had a small effect on the energy resolutions. The average energy resolutions of the 4 detectors measured at 27 y positions along the middle DOI are shown in table 3. The average energy resolutions for detectors 1 to 4 are 15.8%, 14.7%, 15.8%,

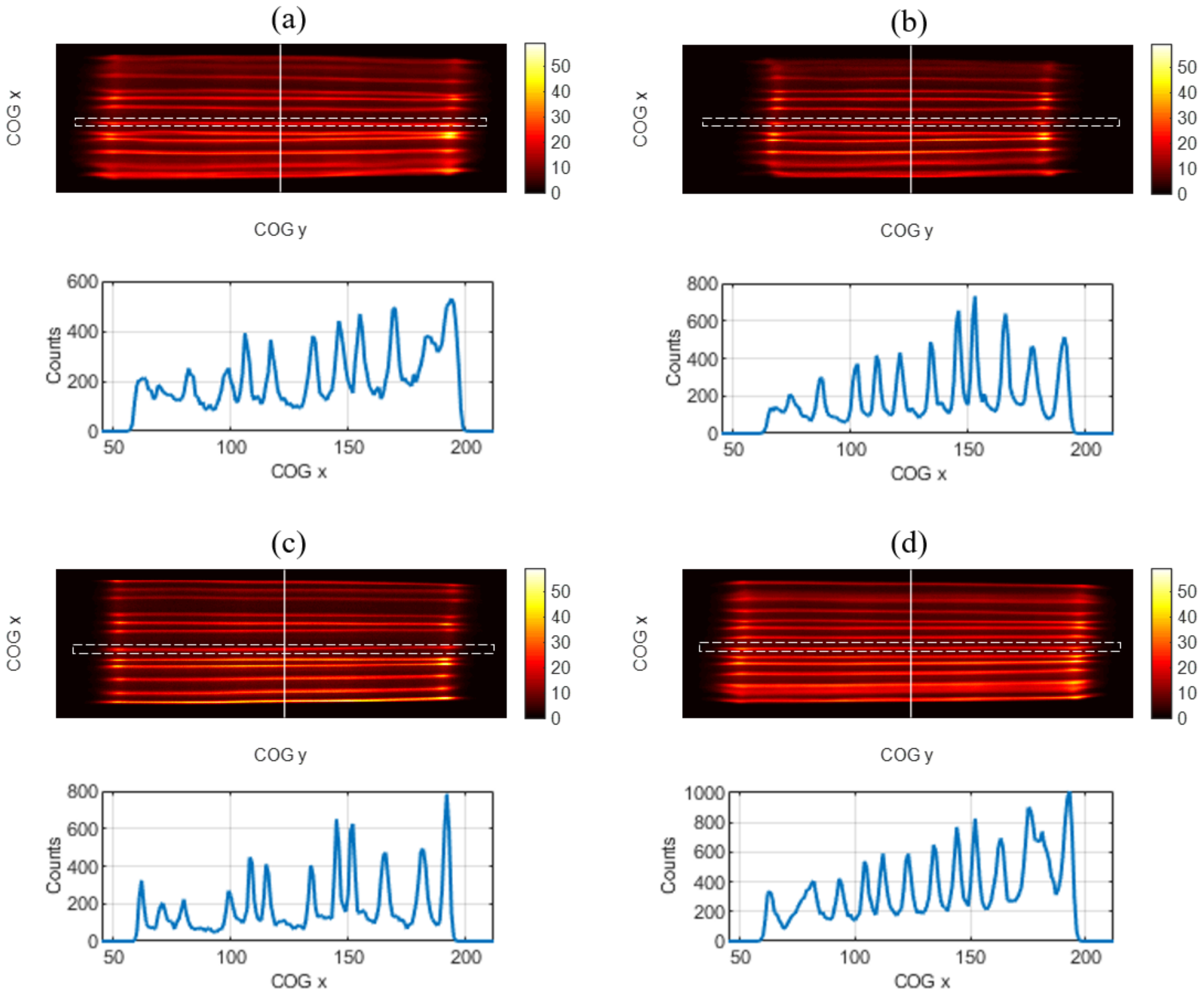

Fig. 6. The flood histograms obtained using the COG method with an energy window of 350-650 keV for detectors (a) 1, (b) 2, (c) 3, and (d) 4. The slab between the two white dashed lines is selected from each detector to plot the energy spectra, y profiles, and DOI profiles.

and 16.4% respectively. Detector 2 (without black paint) has the best energy resolution since the black paint absorbs some scintillation photons, thus degrading the energy resolutions of the other 3 detectors.

C. Spatial resolution in the monolithic direction

The curves of the peak positions of the COG and squared COG algorithms for different y irradiation positions measured at 3 depths are shown in Fig. 8. for detectors 1 and 4. The curves are linear at the middle of the detectors and become non-linear at both ends due to scintillation photon reflection and truncation. The non-linearity decreases as the depth increases. The non-linearity increases the challenge of the detector calibration and degrades the spatial resolution in the monolithic direction. The curves are similar for different slabs of a detector (data is not shown). Fig. 9 shows the y profiles of 27 different y positions and 2 DOIs of detector 1 obtained with the two positioning methods. The horizontal coordinate of the y profiles is converted to mm by using the curves as shown in Fig. 8. For both methods, the profiles' resolvability deteriorates more towards both ends due to the edge effect. To clearly see the effects of the positioning methods and depths on the y spatial resolution, y profiles of DOI of $5\,\mathrm{mm}$ and y of $42\,\mathrm{mm}$ obtained using the COG and squared COG methods, and y profiles of DOIs of 1 and $5\,\mathrm{mm}$ and y of $42\,\mathrm{mm}$ obtained using the squared COG method are shown in Fig. 9 (e), and Fig. 9 (f), respectively.

Fig. 10 shows the spatial resolutions of all irradiation positions of detectors 1 and 4 using the COG and squared COG methods. For both methods, the y spatial resolution improves as the DOI moves toward the SiPM. The y spatial resolution degrades as the y position moves towards both ends due to the edge effects. At the DOI near the SiPM, variation of the y spatial resolution with the changes of the y positions is observed due to the gaps between the SiPM pixels and the inactive areas at the edge of the SiPM pixels. The squared COG method

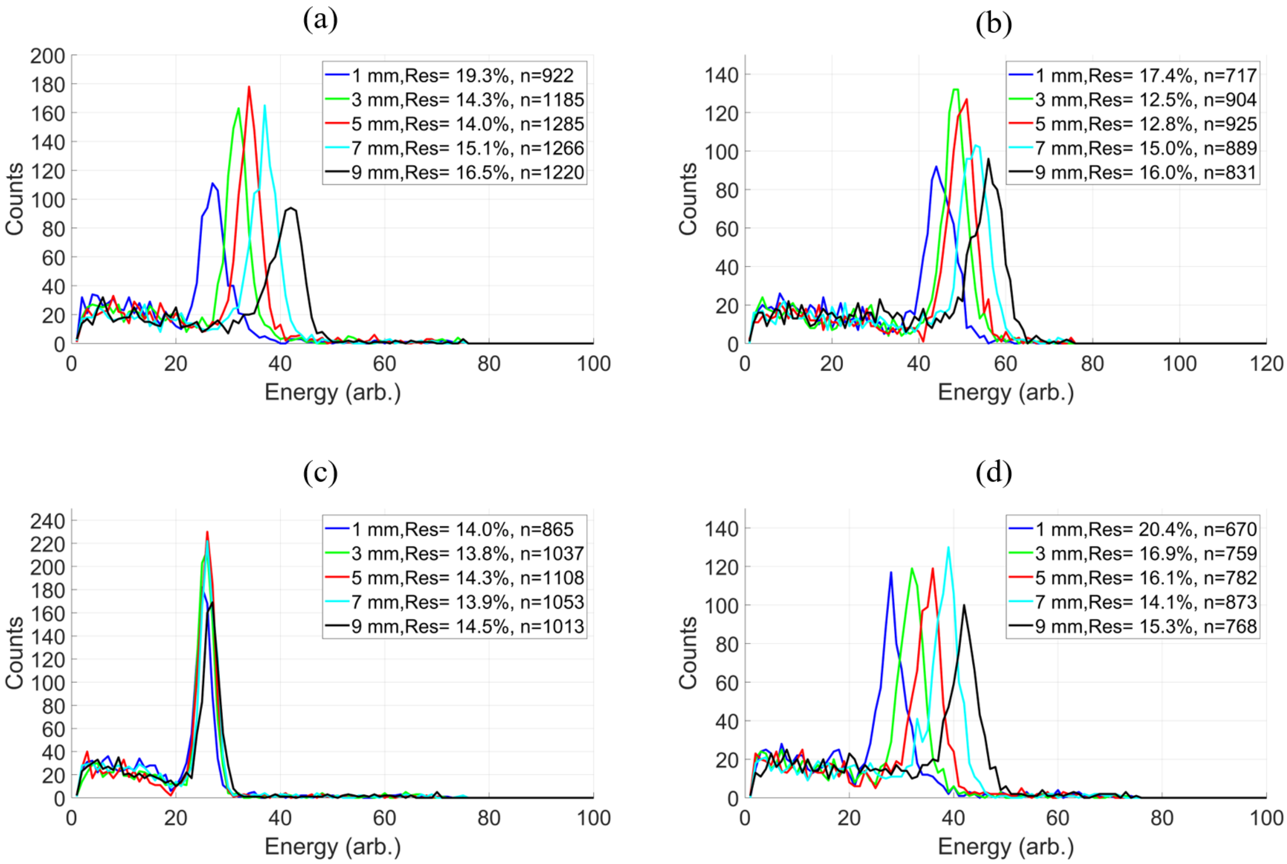

Fig. 7. The energy spectra of a middle slab as shown in Fig. 6 measured at the middle y position and various DOI positions for detectors (a) 1, (b) 2, (c) 3, and (d) 4. n is the number of events of each curve.

shows better y spatial resolution than the COG method. As shown in table 2, the y spatial resolutions averaged over the whole detectors are $1.68{\pm}0.29$ and $1.67{\pm}0.27\,\mathrm{mm}$ for detectors 1 and 4, respectively. As shown in table 3, the average y spatial resolutions measured at depth of $5\,\mathrm{mm}$ are $1.66{\pm}0.16$, $1.87{\pm}0\,31$, $1.71{\pm}0.26$, and $1.67{\pm}0.14\,\mathrm{mm}$ for detectors 1 to 4, respectively.

D. DOI resolution

Fig. 11 shows the DOI profiles of the 4 detectors measured at a center y position ($28\,\mathrm{mm}$). The DOI resolution significantly degraded as the DOI moved away from the SiPM. This is because the change of the scintillation photon distribution width with the DOI becomes smaller as the DOI is farther from the SiPM. Fig. 12 shows the DOI resolutions at all irradiation positions for detectors 1 and 4. The DOI resolution degrades towards both ends of the detector too due to the edge effect. The average DOI resolution results are summarized in tables 2 and 3. The DOI resolutions averaged over the whole detectors are $2.14{\pm}0.76$ and $2.28{\pm}0.67\,\mathrm{mm}$ for detectors 1 and 4, respectively. Detector 2 with unpainted surfaces at the front and both ends provides the worst DOI resolution of $3.41{\pm}2.8\,\mathrm{mm}$ averaged over the 5 DOIs along the center y. The other 3 detectors with black paint at those surfaces provide similar DOI resolution of ~$1.9\,\mathrm{mm}$ averaged over the 5 DOIs along the center y.

E. Timing resolution

Fig. 13 shows the timing resolutions of the detectors 1 and 4. The results of the average timing resolutions of the 4 detectors are shown in tables 2 and 3. The timing resolution of the 4 detectors is similar. The poor timing resolution results of this work resulted from the unoptimized timing pick-off circuit rather than the semi-monolithic scintillator detector since a timing resolution of $<600\,\mathrm{ps}$ had been obtained for a small semi-monolithic detector by using Nuclear Instrument Module electronics[26].

IV. DISCUSSION AND CONCLUSIONS

In this work, the performance of four PET detector modules consisting of semi-monolithic LYSO slabs with different surface treatments, inter-slab reflectors, and slab thicknesses was evaluated by using signal processing electronics developed by our lab. To our knowledge, those were the longest

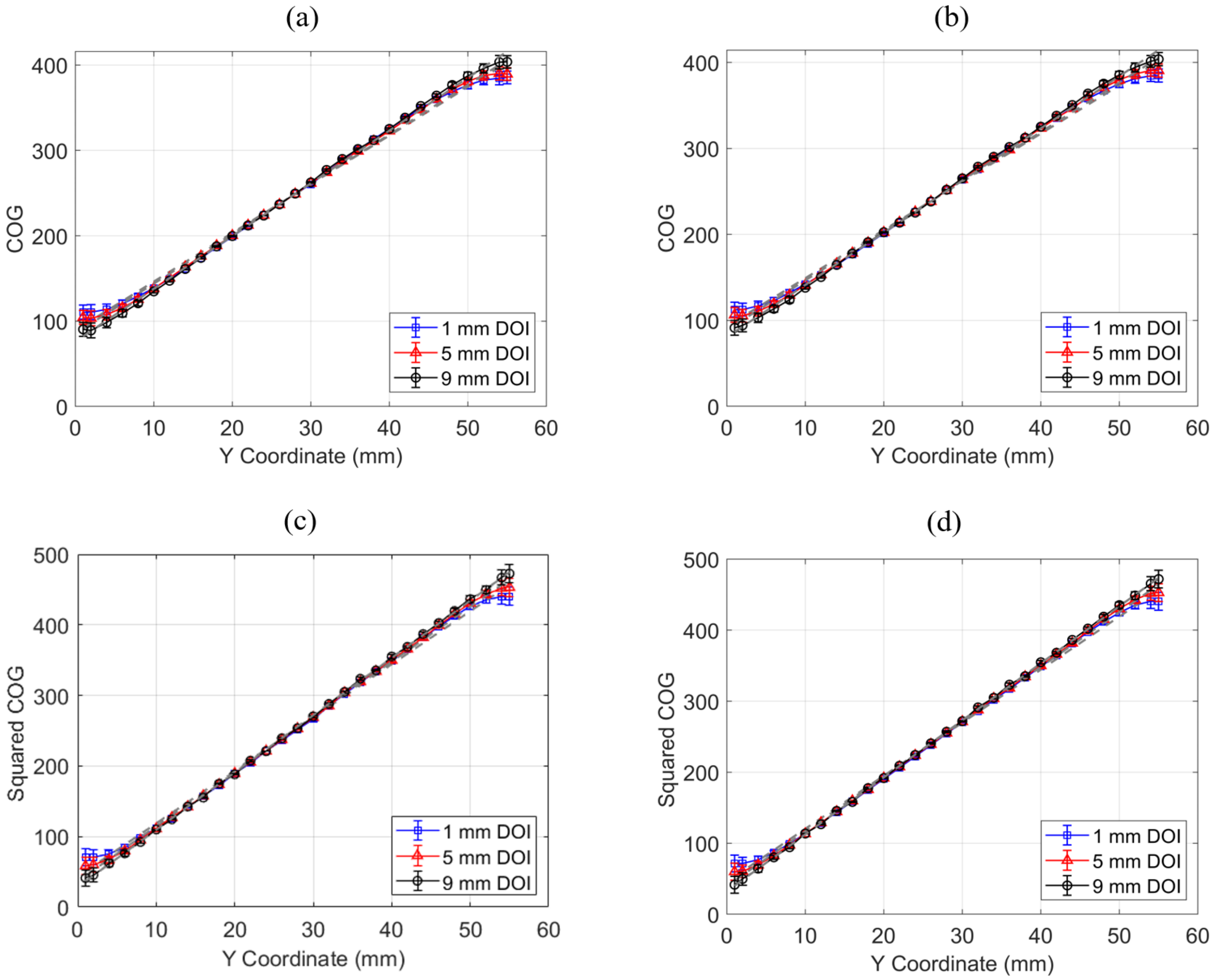

Fig. 8. The peak positions of the measured y histograms vs the true y irradiation positions. (a) Detector 1, COG method, (b) detector 4, COG method, (c) detector 1, squared COG method, and (d) detector 4, squared COG method. The number of events of each position is ~1000.

Table 2. Summary of the results of detectors 1 and 4 averaged over the 27×5 irradiation positions.

Detectors	1	4
y resolution COG (mm)	2.15 ± 0.57	2.12 ± 0.50
y resolution squared COG (mm)	1.68 ± 0.29	1.67 ± 0.27
DOI resolution (mm)	2.14 ± 0.76	2.28 ± 0.67
Energy resolution (%)	17.4 ± 2.4	17.6 ± 2.0
Timing resolution (ns)	3.34 ± 0.49	3.47 ± 0.45

($56\,\mathrm{mm}$) and thinnest ($0.81\,\mathrm{mm}$) semi-monolithic scintillator PET detectors measured up to date. Semi-monolithic scintillator PET detectors using the ESR and $BaSO_4$ reflector were compared for the first time in this work.

Through the use of a lightguide with grooves near both ends, clear slab identification is attained for the 3 detectors using LYSO slabs of $0.96\,\mathrm{mm}$ thick. The second and third slabs at the edges cannot be clearly identified for the detector using $0.81\,\mathrm{mm}$ thick LYSO slabs. The groove positions at the lightguide will be optimized in the future.

Black paint treatment of the two end and front surfaces degrades the energy resolution, but improves both the spatial resolution in the monolithic direction and DOI resolution. The energy resolution is degraded from 14.7% to 15.8%. The spatial resolution in the monolithic direction is improved from $2.65\,\mathrm{mm}$ to $2.15\,\mathrm{mm}$ for the COG method, and from $1.87\,\mathrm{mm}$ to $1.66\,\mathrm{mm}$ for the squared COG method. The DOI resolution is improved from $3.41\,\mathrm{mm}$ to $1.92\,\mathrm{mm}$. Overall, black paint treatment of the crystal surfaces improves the performance of the semi-monolithic PET detectors.

Although the detector using ESR as the inter-slab reflector provides the lowest light output, the photopeak amplitude almost doesn't change with the DOI, which makes the energy calibration of the detector much easier. The detector using ESR reflector provides clearer individual slab identification in the flood histogram, similar spatial resolution at the monolithic direction, DOI resolution, and energy resolution. Over-

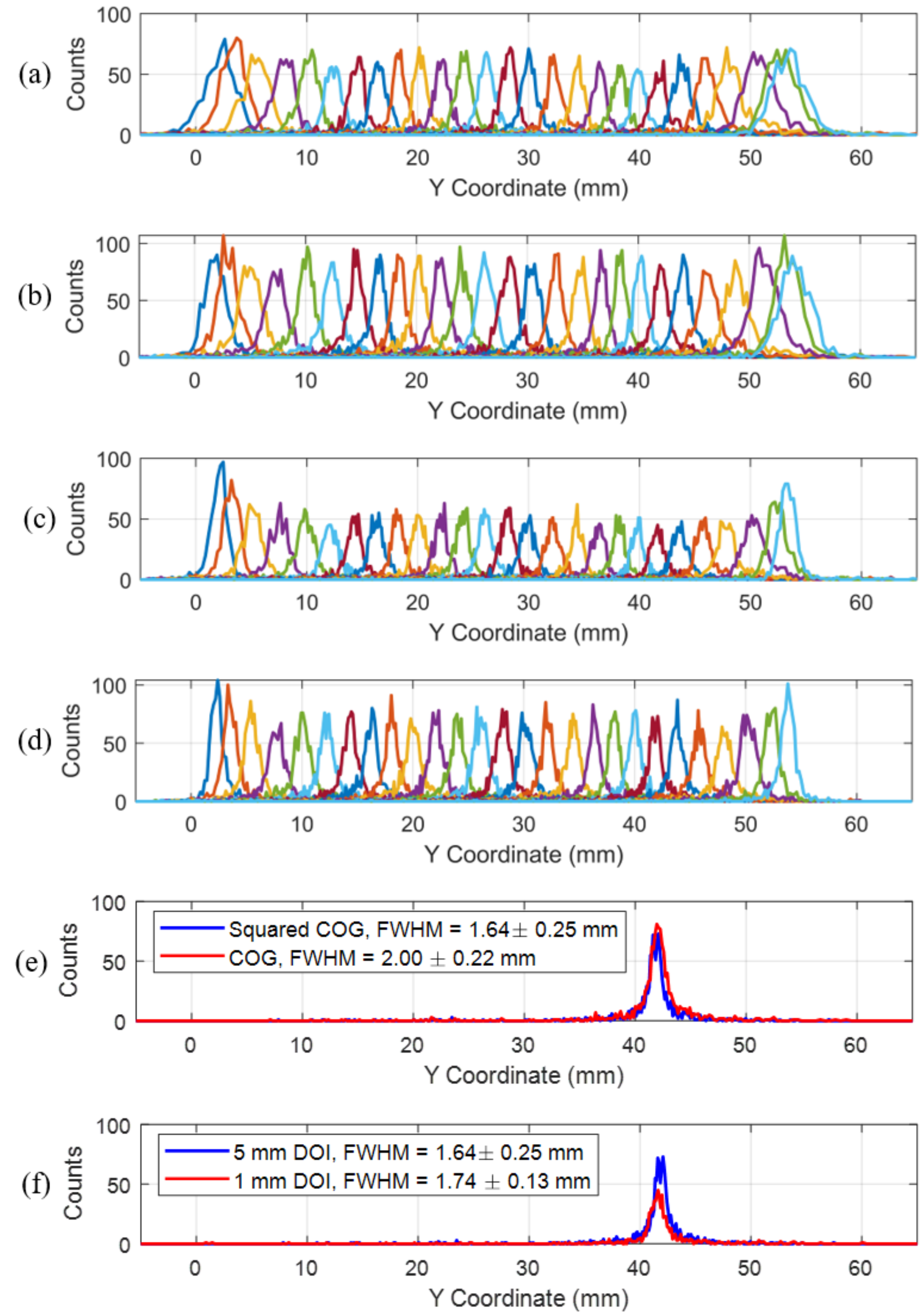

Fig. 9. The y profiles in mm for one middle slab of detector 1 as shown in Fig. 6 (a) the COG method, 1 mm DOI, 27 y positions, (b) the COG method, 5 mm DOI, 27 y positions, (c) squared COG method, 1 mm DOI, 27 y positions, (d) squared COG method, 5 mm DOI, 27 y positions, (e) both methods, 5 mm DOI, 42 mm y, (f) squared COG method, 1 and 5 mm DOIs, 42 mm y. The number of events of each position is ~1000.

all, ESR is a better inter-slab reflector than the $BaSO_4$ reflector.

In this work, a squared COG positioning method was compared with the traditional COG method. The squared COG method gives more weight to the SiPM column signals with high amplitudes and improves the spatial resolution in the monolithic direction by ~30% by reducing the effect of signals with poor signal-to-noise ratio. The squared COG method can also be easily implemented in modern PET electronics.

Currently, both pixelated and monolithic scintillator detectors have been used in developing high-resolution small animal and organ-specific PET scanners. The semi-monolithic detectors present a suitable alternative to those detectors since the edge effect is smaller as compared to the monolithic detectors and the DOI can be measured with single-ended read-

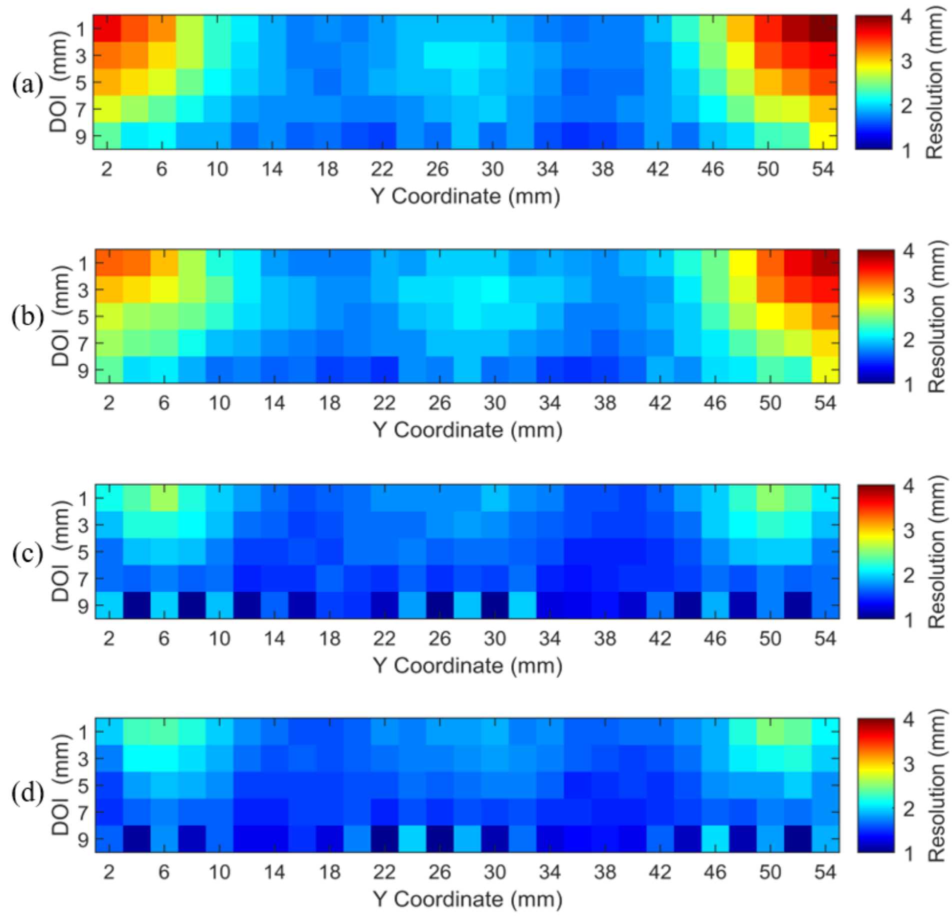

Fig. 10. The y spatial resolutions of all irradiation positions. (a) Detector 1, COG method, (b) detector 4, COG method, (c) detector 1, squared COG method, and (d) detector 4, squared COG method. The counts of each irradiation position is ~1000 per slab.

Table 3. Summary of the results for all 4 detectors. The y spatial resolution and energy resolution are averaged over the 27 irradiation positions along the center DOI. The DOI resolution is averaged over the 5 irradiation positions along the center y.

Detectors	1	2	3	4
y resolution COG (mm)	2.15 ± 0.57	2.65 ± 0.80	2.45 ± 0.69	2.13 ± 0.42
y resolution squared COG (mm)	1.66 ± 0.16	1.87 ± 0.31	1.71 ± 0.26	1.67 ± 0.14
DOI resolution (mm)	1.92 ± 0.51	3.41 ± 2.80	1.94 ± 0.47	1.87 ± 0.47
Energy resolution (%)	15.8 ± 2.2	14.7 ± 1.3	15.8 ± 0.9	16.4 ± 1.3
Timing resolution (ns)	3.29 ± 0.53	3.09 ± 0.47	3.39 ± 0.50	3.38 ± 0.48

out as compared to pixelated scintillator detectors that need dual-ended readout or more complex detector designs. The cost of the semi-monolithic scintillator is lower than that of the pixelated detector, but higher than that of the monolithic detector. In the future, SiPM array with smaller gaps among pixels will be used, the crystal surface treatments will be further optimized and a machine learning-based positioning algorithm will be developed to improve the resolutions in both the monolithic and DOI directions. Semi-monolithic scintillator detectors with thinner slabs and using the ESR reflector will be evaluated. Advanced signal processing techniques will be studied to improve the timing resolution of the detector and explore the possibility of using the semi-monolithic scintillator detectors for time-of-flight PET scanners.

In summary, the long semi-monolithic scintillator detectors optimized in this work provide a clear identification of LYSO slabs of 0.96 and $0.81\,\mathrm{mm}$ thick, a spatial resolution in the monolithic direction of ~$1.7\,\mathrm{mm}$ by using the squared COG method, a DOI resolution of ~$1.9\,\mathrm{mm}$, and energy resolutions of ~16%. Since the irradiation beam width of ~$1\,\mathrm{mm}$ is not subtracted from the measured results, the true spatial resolution in the monolithic direction and the DOI resolution are

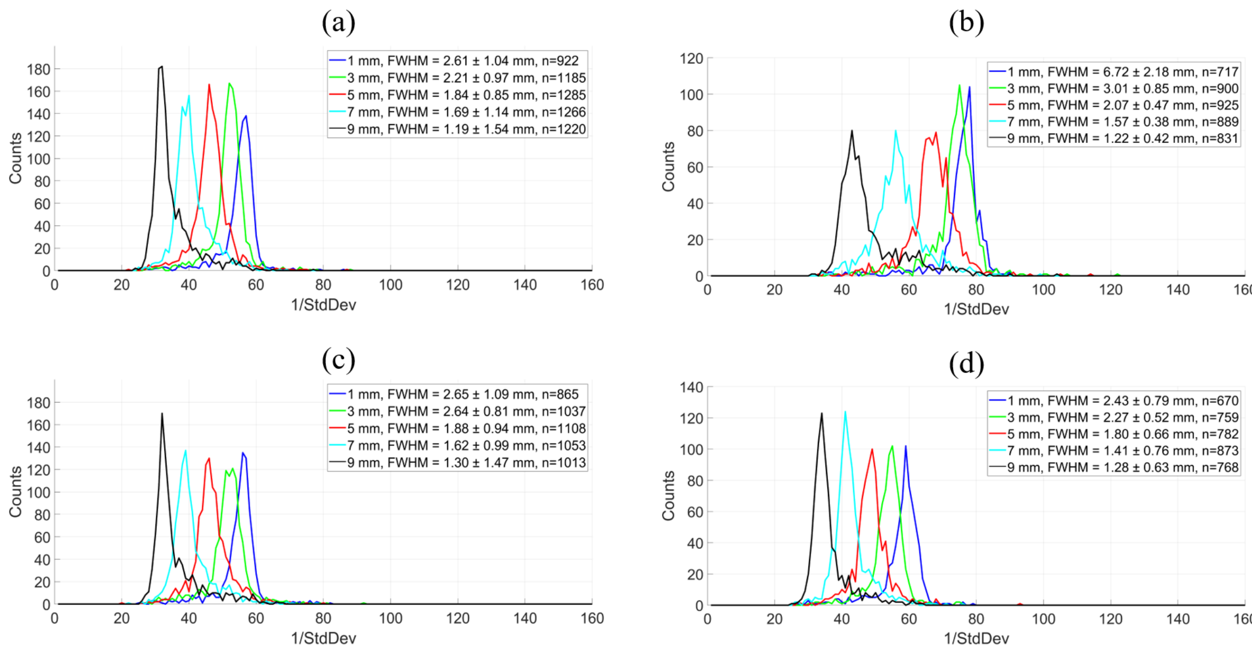

Fig. 11. The DOI profiles of a middle slab as shown in Fig. 6 measured for a y position of $28\,\mathrm{mm}$ and depths of 1, 3, 5, 7, and $9\,\mathrm{mm}$ for detectors (a) 1, (b) 2, (c) 3 and (d) 4. n is the number of events of each curve.

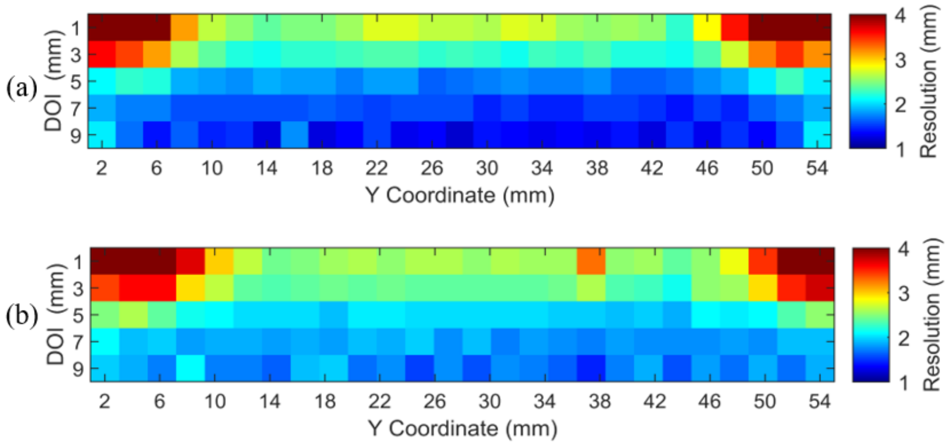

Fig. 12. The DOI resolutions at all irradiated positions of detectors (a) 1 and (b) 4. The number of events of each irradiation position is ~1000 per slab.

even better. Based on the achieved performance, the detectors can be used to develop high-performance small animal and organ-specific PET scanners in the future.

V. BIBLIOGRAPHY

[1] S.R. Cherry, T. Jones, J.S. Karp et al., Total-Body PET: Maximizing Sensitivity to Create New Opportunities for Clinical Research and Patient Care. J. Nucl. Med. **59**, 3-12 (2018). doi: 10.2967/jnumed.116.184028

[2] S. Vandenberghe, P. Moskal, J.S. Karp, State of the art in total body PET. EJNMMI Phys. **7**, 1-33 (2020). doi: 10.1186/s40658-020-00290-2

[3] V. Bettinardi, I. Castiglioni, E. De Bernardi et al., PET quan-

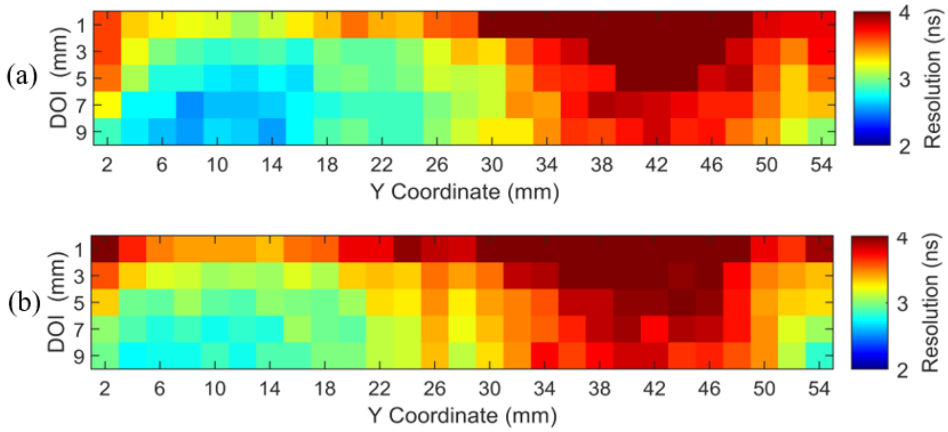

Fig. 13. The timing resolutions at all irradiated positions of detectors (a) 1 and (b) 4. The number of events of each irradiation position is ~1000 per slab.

tification: strategies for partial volume correction. Clin Transl Imaging. **2**, 199-218 (2014). doi: 10.1007/s40336-014-0066-y

[4] Y. Yang, J. Bec, J. Zhou et al., A Prototype High-Resolution Small-Animal PET Scanner Dedicated to Mouse Brain Imaging. J. Nucl. Med. **57**, 1130-1135 (2016). doi: 10.2967/jnumed.115.165886

[5] R.S. Miyaoka, A.L. Lehnert, Small animal PET: a review of what we have done and where we are going. Phys. Med. Biol. **65**, 24TR04 (2020). doi: 10.1088/1361-6560/ab8f71

[6] J. Du, T. Jones, Technical opportunities and challenges in developing total-body PET scanners for mice and rats. EJNMMI Phys. **10**, 2 (2023). doi: 10.1186/s40658-022-00523-6

[7] A. Verger, A. Kas, J. Darcourt et al., PET Imaging in Neuro-Oncology: An Update and Overview of a Rapidly Growing Area. Cancers. **14**, 1103 (2022). doi: 10.3390/cancers14051103

[8] C. Catana, Development of Dedicated Brain PET Imaging Devices: Recent Advances and Future Perspectives. J. Nucl. Med. **60**, 1044-1052 (2019). doi: 10.2967/jnumed.118.217901

[9] S. Vandenberghe, E. Mikhaylova, E. D'Hoe et al., Recent developments in time-of-flight PET. EJNMMI Phys. **3**, 3 (2016). doi: 10.1186/s40658-016-0138-3

[10] J. Van Sluis, J. De Jong, J. Schaar et al., Performance Characteristics of the Digital Biograph Vision PET/CT System. J. Nucl. Med. **60**, 1031-1036 (2019). doi:10.2967/jnumed.118.215418

[11] L. Eriksson, K. Wienhard, M. Eriksson et al., The ECAT HRRT: NEMA NEC evaluation of the HRRT system, the new high-resolution research tomograph. IEEE T. Nucl. Sci. **49**, 2085-2088 (2002). doi: 10.1109/TNS.2002.803784

[12] N. Inadama, H. Murayama, M. Hamamoto et al., 8-Layer DOI Encoding of 3-Dimensional Crystal Array. IEEE T. Nucl. Sci. **53**, 2523-2528 (2006). doi: 10.1109/TNS.2006.882795

[13] Y. Yang, P.A. Dokhale, R.W. Silverman et al., Depth of interaction resolution measurements for a high resolution PET detector using position sensitive avalanche photodiodes. Phys. Med. Biol. **51**, 2131-2142 (2006). doi: 10.1088/0031-9155/51/9/001

[14] Z. Kuang, X. Wang, N. Ren et al., Design and performance of SIAT aPET: a uniform high-resolution small animal PET scanner using dual-ended readout detectors. Phys. Med. Biol. **65**, 235013 (2020). doi: 10.1088/1361-6560/abbc83

[15] Z. Gu, R. Taschereau, N.T. Vu et al., Performance evaluation of HiPET, a high sensitivity and high resolution preclinical PET tomograph. Phys. Med. Biol. **65**, 045009 (2020). doi: 10.1088/1361-6560/ab6b44

[16] P. Bruyndonckx, S. Leonard, S. Tavernier et al., Neural network-based position estimators for PET detectors using monolithic LSO blocks. IEEE T. Nucl. Sci. **51**, 2520-2525 (2004). doi: 10.1109/TNS.2004.835782

[17] M.C. Maas, D.J. van der Laan, D.R. Schaart et al., Experimental characterization of monolithic-crystal small animal PET detectors read out by APD arrays. IEEE T. Nucl. Sci. **53**, 1071-1077 (2006). doi: 10.1109/TNS.2006.873711

[18] M. Balcerzyk, G. Kontaxakis, M. Delgado et al., Initial performance evaluation of a high resolution Albira small animal positron emission tomography scanner with monolithic crystals and depth-of-interaction encoding from a user's perspective. Meas. Sci. Technol. **20**, 104011 (2009). doi: 10.1088/0957-0233/20/10/104011

[19] S. Krishnamoorthy, E. Blankemeyer, P. Mollet et al., Performance evaluation of the MOLECUBES β-CUBE–a high spatial resolution and high sensitivity small animal PET scanner utilizing monolithic LYSO scintillation detectors. Phys. Med. Biol. **63**, 155013 (2018). doi: 10.1088/1361-6560/aacec3

[20] W. Gsell, C. Molinos, C. Correcher et al., Characterization of a preclinical PET insert in a 7 tesla MRI scanner: beyond NEMA testing. Phys. Med. Biol. **65**, 245016 (2020). doi: 10.1088/1361-6560/aba08c

[21] G. Borghi, V. Tabacchini, D.R. Schaart, Towards monolithic scintillator based TOF-PET systems: practical methods for detector calibration and operation. Phys. Med. Biol. **61**, 4904-4928 (2016). doi: 10.1088/0031-9155/61/13/4904

[22] M. Stockhoff, R.V. Holen, S. Vandenberghe, Optical simulation study on the spatial resolution of a thick monolithic PET detector. Phys. Med. Biol. **64**, 195003 (2019). doi: 10.1088/1361-6560/ab3b83

[23] G. Borghi, V. Tabacchini, S. Seifert et al., Experimental validation of an efficient fan-beam calibration procedure for k-nearest neighbor position estimation in monolithic scintillator detectors. IEEE T. Nucl. Sci. **62**, 57-67 (2015). doi:

10.1109/TNS.2014.2375557

[24] Y.H. Chung, S.J. Lee, C.H. Baek et al., New design of a quasi-monolithic detector module with DOI capability for small animal pet. Nucl. Instrum. Meth. A. **593**, 588-591 (2008). doi:10.1016/j.nima.2008.05.059

[25] Y.H. Chung, C.H. Baek, S.J. Lee et al., Preliminary experimental results of a quasi-monolithic detector with DOI capability for a small animal PET. Nucl. Instrum. Meth. A. **621**, 590-594 (2010). doi: 10.1016/j.nima.2010.04.039

[26] X. Zhang, X. Wang, N. Ren et al., Performance of a SiPM based semi-monolithic scintillator PET detector. Phys. Med. Biol. **62**, 7889-7904 (2017). doi: 10.1088/1361-6560/aa898a

[27] Z. Kuang, X. Wang, C. Li, et al., Performance of a high-resolution depth encoding PET detector using barium sulfate reflector. Phys. Med. Biol. **62**, 5945-5958 (2017). doi: 10.1088/1361-6560/aa71f3

[28] X. Zhang, X. Wang, N. Ren et al., Performance of long rectangular semi-monolithic scintillator PET detectors. Med. Phys. **46**, 1608-1619 (2019). doi: 10.1002/mp.1343

[29] Y. Kuhl, F. Mueller, S. Naunheim et al., A finely segmented semi-monolithic detector tailored for high-resolution PET. Med. Phys. **51**, 3421-3436 (2024). doi: 10.1002/mp.16928

[30] N. Cucarella, J. Barrio, E. Lamprou et al., Timing evaluation of a PET detector block based on semi-monolithic LYSO crystals. Med. Phys. **48**, 8010-8023 (2021). doi: 10.1002/mp.15318

[31] C. Zhang, X. Wang, M. Sun et al., A thick semi-monolithic scintillator detector for clinical PET scanners. Phys. Med. Biol. **66**, 065023 (2021). doi: 10.1088/1361-6560/abe761

[32] F. Mueller, S. Naunheim, Y. Kuhl et al., A semi-monolithic detector providing intrinsic DOI-encoding and sub-200 ps CRT TOF-capabilities for clinical PET applications. Med. Phys. **49**, 7469-7488 (2022). doi: 10.1002/mp.16015

[33] M. Freire, J. Barrio, N. Cucarella et al., Position estimation using neural networks in semi-monolithic PET detectors. Phys. Med. Biol. **67**, 245011 (2022). doi: 10.1088/1361-6560/aca389

[34] A. Iborra, A.J. González, A.G. Montoro et al., Ensemble of neural networks for 3D position estimation in monolithic PET detectors. Phys. Med. Biol. **64**, 195010 (2019). doi: 10.1088/1361-6560/ab3b86

[35] Z. Kuang, Z. Sang, N. Ren et al., Development and performance of SIAT bPET: a high-resolution and high-sensitivity MR-compatible brain PET scanner using dual-ended readout detectors. Eur. J. Nucl. Med. Mol. I. **51**, 346-357 (2024). doi: 10.1007/s00259-023-06458-z

[36] J. Lu, L. Zhao, K. Chen et al., Real-time FPGA-based digital signal processing and correction for a small animal PET. IEEE T. Nucl. Sci. **66**, 1287-1295 (2019). doi: 10.1109/TNS.2019.2908220

[37] L. Zhao, C. Ma, S. Chu et al., Prototype of the Readout Electronics for WCDA in LHAASO. IEEE T. Nucl. Sci. **64**, 1367-1373 (2017). doi: 10.1109/TNS.2017.2693296

[38] P. Deng, L. Zhao, J. Lu et al., Prototype design of singles processing unit for the small animal PET. J. Instrum. **13**, T05007 (2018). doi: 10.1088/1748-0221/13/05/T05007

[39] K. Chen, L. Zhao, L. Zhang et al., Testing of Singles Processing Unit for a Brain PET. 2021 IEEE Nuclear Science Symposium and Medical Imaging Conference (NSS/MIC). 1-3 (2021). doi: 10.1109/NSS/MIC44867.2021.9875447

[40] D. Schug, J. Wehner, B. Goldschmidt et al., Data processing for a high resolution preclinical PET detector based on Philips DPC digital SiPMs. IEEE T. Nucl. Sci. **62**, 669-678 (2015). doi: 10.1109/TNS.2015.2420578